Residual Stress and Ferroelastic Domain Reorientation in Declamped {001} $Pb(Zr_{0.3}Ti_{0.7})O_3$ Films

Lyndsey M. Denis-Rotella, *Member, IEEE*, Giovanni Esteves, Julian Walker, Hanhan Zhou, *Associate Member, IEEE*, Jacob L. Jones, *Fellow, IEEE*, and Susan Trolier-McKinstry, *Fellow, IEEE*

***Abstract*— Ferroelectric films are often constrained by their substrates and subject to scaling effects, including suppressed dielectric permittivity. In this work, the thickness dependence of intrinsic and extrinsic contributions to the dielectric properties was elucidated. A novel approach to quantitatively deconstruct the relative permittivity into three contributions (intrinsic, reversible extrinsic, and irreversible extrinsic) was developed using a combination of X-ray diffraction (XRD) and Rayleigh analysis. *In situ* synchrotron XRD was used to understand the influence of residual stress and substrate clamping on the domain state, ferroelastic domain reorientation, and electric field-induced strain. For tetragonal {001} textured $Pb_{0.99}(Zr_{0.3}Ti_{0.7})_{0.98}Nb_{0.02}O_3$ thin films clamped to an Si substrate, a thickness-dependent in-plane tensile stress developed during processing, which dictates the domain distribution over a thickness range of 0.27–1.11 μm. However, after the films were partially declamped from the substrate and annealed, the residual stress was alleviated. As a result, the thickness dependence of the volume fraction of *c*-domains largely disappeared, and the out-of-plane lattice spacings (*d*) for both *a*- and *c*-domains increased. The volume fraction of *c*-domains was used to calculate the intrinsic relative permittivity. The reversible Rayleigh coefficient was then used to separate the intrinsic and reversible extrinsic contributions. The reversible extrinsic response accounted for ~50% of the overall relative permittivity (measured at 50 Hz and alternating current (ac) field of 0.5·E_c) and was thickness dependent even after poling and upon release.**

Manuscript received January 30, 2020; accepted April 8, 2020. Date of publication April 13, 2020; date of current version January 26, 2021. This work was supported in part by the National Science Foundation under Grant DMR-1410907, Grant DMR-1409399, and Grant DGE-1255832, in part by the U.S. Army Research Office, in part by the National Science Foundation Graduate Research Fellowship Program, and in part by the Alfred P. Sloan Foundation under Grant G-2016-20166039. The use of the Advanced Photon Source at Argonne National Laboratory was supported by the U.S. Department of Energy under Contract DE-AC02-06CH11357. *(Corresponding author: Lyndsey M. Denis-Rotella.)*

Lyndsey M. Denis-Rotella and Susan Trolier-McKinstry are with the Materials Science and Engineering Department, Materials Research Institute, Pennsylvania State University, University Park, PA 16802-1503 USA (e-mail: set1@psu.edu).

Giovanni Esteves, Hanhan Zhou, and Jacob L. Jones are with the Department of Materials Science and Engineering, North Carolina State University, Raleigh, NC 27607 USA.

Julian Walker is with the Materials Science and Engineering Department, Norwegian University of Science and Technology, 7491 Trondheim, Norway.

This article has supplementary downloadable material available at https://ieeexplore.ieee.org, provided by the authors.

Digital Object Identifier 10.1109/TUFFC.2020.2987438

***Index Terms*— Domain wall motion, residual stress, substrate clamping, thin films, X-ray diffraction (XRD).**

I. Introduction

FERROELECTRIC materials are utilized in applications such as actuators, sensors, and nonvolatile memory [1]. Typically, the dielectric and piezoelectric responses in ferroelectric thin films are suppressed relative to their bulk counterparts due to a combination of small grain sizes, thermal strains, clamping due to the substrate, and the potential for a high concentration of defects [2]–[7].

In ferroelectrics, residual stresses can dictate preferred domain distributions [8]. In many ferroelectric films, the substrate has a strong influence on the domain configuration [9]. For example, preferential out-of-plane polarization can be achieved for relaxed, tetragonal $Pb(Zr_x, Ti_{1-x})O_3$ (PZT) films grown on sapphire, MgO, or $LaAlO_3$, which have a larger coefficient of thermal expansion compared with PZT [7]–[11]. This type of domain configuration is ideal for applications such as FeRAM which utilize out-of-plane polarization switching for memory [12].

Since the coefficient of thermal expansion (α_{CTE}) of Si (2.6 ppm/°C) is less than that of PZT in the paraelectric phase (6.7–9.4 ppm/°C, depending on composition) [8], PZT films processed on Si experience in-plane tensile stress, favoring orientation of the spontaneous polarization in-plane (e.g., producing preferentially *a*-domain rather than *c*-domain films) [10], [13]. Moreover, local stresses can form at the film–bottom electrode interface that differ from the average residual stress, complicating the understanding. Griggio *et al.* [14] proposed that these local strains can be partially relieved by removing the film from the substrate. The residual stress state of PZT films on Si is also reported to depend on the number of deposited layers or film thickness [15] and is correlated with variations in domain patterns [16], [17]. The dependence of the stress state on film thickness may also be associated with changes in the stress state of the underlying thermal oxide layer or Pt-bottom electrode during subsequent annealing [18], [19].

Differences in the intrinsic and extrinsic contributions to the relative permittivity (ε_r) will result from differences in the domain orientation state, domain wall densities, and the mobility of domain walls. This, in turn, contributes to the apparent

scaling effects in the functional properties [4], [20], [21]. For example, PZT films which have predominately a-domains will have a larger out-of-plane intrinsic contribution to ε_r, possibly at the expense of a reduced 90° domain wall density and reduced extrinsic contributions to ε_r [9]. Therefore, variations in the in-plane stress state of PZT films can result in a thickness dependence in the domain state, intrinsic contributions, and extrinsic contributions to ε_r.

The differences in the intrinsic and extrinsic contributions to ε_r can often be quantified using Rayleigh analysis [21]–[25]. The Rayleigh law, as in (1), describes a linear relationship between the ε_r and an alternating current (ac)-driven electric field of amplitude E_0

$$\varepsilon_r = \varepsilon_{\text{initial}} + \alpha_\varepsilon E_0. \tag{1}$$

In (1), $\varepsilon_{\text{initial}}$ is the reversible dielectric Rayleigh coefficient and represents the sum of reversible extrinsic and intrinsic contributions to the permittivity. α_ε is the irreversible dielectric Rayleigh coefficient associated with extrinsic contributions to the permittivity from irreversible movement of domain walls and phase boundaries through a random potential energy landscape [26]. Rayleigh analysis cannot differentiate between motion of 90° and 180° domain walls. Therefore, it is advantageous to couple Rayleigh analysis with another characterization technique, such as *in situ* X-ray diffraction (XRD), that can directly probe the intrinsic and ferroelastic extrinsic contributions to the permittivity [10], [27]–[29].

The extent of electric field-induced 90° domain reorientation in most clamped PZT films is relatively small compared with bulk ceramics [30], and a majority of the reoriented domains relax back to a remanent state as the electric field decreases to zero [27], [31]. Clamping effects can be alleviated in a variety of ways that are dictated by device design and etching techniques. For example, decreasing the width:thickness aspect ratio of the piezoelectric layer can partially declamp the film and enhance piezoelectric properties [32]–[34]. Alternatively, removing the substrate via an undercut release process can also relax substrate clamping effects [14], [25], [29].

Griggio *et al.* [14] proposed that removing the substrate from underneath the film can alleviate residual stress at the film–substrate interface and may relax thermal stresses by bending. However, Wallace *et al.* [29] observed no significant changes in the volume fraction of c-domains (ν_{002}) normal to the film surface on release of elongated diaphragms with 2-μm-thick tetragonal PZT films. Therefore, simply releasing the film from the substrate may not change the average residual stress enough to induce a change in the overall domain distribution of the film for thick, taut membranes [29]. Notably, these studies were limited to comparatively thick PZT films (>1 μm) in which the film–substrate interface makes up a small fraction of the overall film thickness. For thinner films, Berfield *et al.* [5] attributed a substantial reduction in polarizability of sol–gel-derived PZT films <200 nm in thickness to higher residual stress than that observed in thicker films. Therefore, alleviating the residual stress at the film–substrate interface may have a larger effect on the domain distribution in thinner films (<1 μm).

If stress was the dominant effect that degrades properties in thin ferroelectric films, then it would be expected that the properties of thin films would be most affected by the removal of both substrate clamping and residual stresses. Alternatively, if the defect concentration in thinner films (e.g., due to lead loss to the bottom electrode or smaller grain size) was to dominate the property suppression, then reduction of substrate clamping would be expected to produce a less-pronounced improvement in properties. Further investigation is required to assess which effect is dominant.

In this work, *in situ* high-resolution XRD was used to directly probe the structure of ferroelectric thin films and assess the effect of substrate clamping and residual stress on the thickness dependence of the domain state, strain, and domain reorientation of PZT films for thicknesses ranging from 0.27 to 1.11 μm. The results confirm that the properties of thin clamped films are influenced by both the stress and the defect chemistry. The combination of XRD and Rayleigh analysis allowed, for the first time, deconvolution of the intrinsic and the reversible, extrinsic contributions to the dielectric permittivity. This, in turn, permits a better understanding of the mechanisms governing size effects in thin films.

II. Experimental Procedure

A. Film Synthesis and Nanofabrication

Details of the chemical solution deposition process used and the layer-by-layer fabrication can be found elsewhere [21], [35], [36]. In short, tetragonal {001} textured $Pb(Zr_{0.3}Ti_{0.7})O_3$ (PZT 30/70) thin films doped with 2% Nb and thicknesses ranging from 0.27 to 1.11 μm were grown on a $Pt/TiO_2/SiO_2/Si$ stack with corresponding thicknesses of 0.1/0.035/0.5 μm for the $Pt/TiO_2/SiO_2$ stack, respectively. A 0.08M PbO sol–gel was initially spin coated onto the Pt bottom electrode and pyrolyzed to compensate for lead loss to the substrate during crystallization of PZT. Additionally, a commercial PZT-E1 sol–gel solution (Mitsubishi Materials Corporation, Tokyo, Japan) of composition $Pb(Zr_{0.3}Ti_{0.7})O_3$ doped with 10 mol% Pb excess and 1 mol% Mn was used as a seed layer to promote {001} texture. Each subsequent layer was spin coated using 0.4M PZT 30/70 solution with 12 mol% Pb excess and 2 mol% Nb, dried (2 min at 250 °C), pyrolyzed (5 min at 400 °C), and crystallized in a rapid thermal annealer (RTA) (1 min at 700 °C in flowing O_2 gas at 2 standard liter per minute (SLPM) and a ramp rate of 10 °C/s). Each PZT layer crystallized is approximately 80 nm in thickness when deposited using a spin speed of 1500 r/min. This process was repeated until the desired overall film thickness was obtained. The long pyrolysis step enabled the growth of high-density films with lateral grain sizes of 50–150 nm. The average grain sizes of all film thicknesses, as measured by a line intercept method [37], are largely independent of the film thickness, as listed in Table I. Lotgering factors for {001} reflections ranged from 90% to 100% depending on film thickness [38].

Photolithography was used to define top electrode areas and regions on the electrodes subject to a top-down etch and undercut release process. RF magnetron-sputtered platinum top electrodes were defined in 3.5 mm × 0.7 mm areas. Large electrode areas were needed to ensure that an adequate volume of irradiated material was available for actuation during *in situ* XRD measurements. As described elsewhere,

TABLE I
MICROSTRUCTURE AND ELECTRICAL PROPERTIES FOR CLAMPED PZT 30/70 FILMS

Thickness (μm)	P_r (μC/cm^2) [a]	P_{max} (μC/cm^2) [a]	E_c (kV/cm)	ε_r	Loss %	Columnar Grain Size (nm)
1.11±0.002	18.1±0.2	40.0±1.2	62.5±1.4	685±1.2	1.5±0.07	134±13
0.56±0.005	14.1±1.2	37.9±1.8	55.5±4.5	761±2.7	2.2±0.05	97±7
0.38±0.001	12.6±1.3	36.8±0.7	54.1±2.6	730±1.4	2.9±0.05	101± 6
0.27±0.010	11.1±0.2	36.5±0.5	59.2±1.0	738±5.2	3.2±0.2	117±7

[a](P_r and P_{max} measured at 400 kV/cm)

the electrodes were rotated 15° from the [001] of the silicon wafer to minimize diffraction from the substrate [29]. An Ulvac NE-550 inductively coupled high-density plasma etcher was used to dry etch 600 μm × 146 μm pits through the Pt/PZT/Pt/TiO_2/SiO_2 stack, exposing the Si substrate. Top-down etching was continued using an isotropic Xactic XeF_2 e1 vapor etch tool to etch 100-μm-wide trenches into the Si substrate, as described elsewhere [14], [21], [29]. A "75% release" corresponds to an electroded region in which 75% of the Pt/PZT/PT/TiO_2/SiO_2 stack is suspended above a void in the Si substrate. The term "clamped" refers to an electroded region in which no etch trenches or etch pits are present, and the film is fully clamped to the Si substrate. The electrical properties are summarized in Table I for all film thicknesses in the clamped state.

B. X-Ray Measurements and Analysis

To study the domain reorientation at high fields, *in situ* synchrotron XRD measurements were performed at the Advanced Photon Source beamline 11-ID-C with an energy of 105.091 keV (0.117418 Å). The samples were mounted on a custom stage, which allows for *in situ* use of electrical probes with voltage produced by a Keithley 2410C 1100-V source meter. To increase the diffracting volume, the sample was tilted 1° to the incident beam with slit sizes of 0.5 mm in the horizontal direction and 0.05 mm in the vertical direction. As such, the spot size of the beam (2.86 mm × 0.5 mm) was well within the electroded region after alignment. Care was taken to align the electroded area of interest to ensure that only actuated film was captured in the diffracted pattern.

Diffraction patterns were measured while applying a dc electric field. The samples were subjected to annealing at 400 °C for 30 min and aging for at least 24 h prior to measuring XRD patterns to ensure that the domain state of the material was reset to a randomized potential energy landscape. While taking XRD patterns, each film was electrically cycled twice, using the applied voltage sequence shown in Fig. 1(a). During the first cycle, the initial pattern was taken at 0 V and subsequent patterns were taken after the field was increased by steps of $0.25{\cdot}E_c$ (where E_c is the coercive field) until the maximum of $1.5{\cdot}E_c$ was reached. At each step, the applied field was held for 210 s, followed by a 210-s acquisition of a diffraction pattern. Subsequently, patterns were also taken after the applied field was decreased by steps of $0.5{\cdot}E_c$, with the final pattern taken at 0 V. This process was repeated for the second cycle, in which patterns were acquired at increasing field steps of $0.5{\cdot}E_c$ until $3{\cdot}E_c$ was reached. Subsequently, patterns were also taken in decreasing field steps of $1{\cdot}E_c$ until 0 V was reached.

Line profiles were extracted from the measured 2-D diffraction patterns using the Fit2D software (European Radiation Synchrotron Facility, Grenoble, France) [39]. CeO_2 powder (NIST 674b) was used to calibrate the X-ray beam center and sample-to-detector distance, from which lattice (d)-spacing values were calculated. A sector of the 2-D diffraction pattern that represented scattering vectors approximately parallel to the applied electric field direction [the vertical section shown in Fig. 1(b)] was integrated using Fit2D. The width of the integration range was 20°. An example of the extracted line profiles within a limited 2θ range is plotted in Fig. 1(c), highlighting the changes in peak intensity of the 002 and 200 reflections as a function of applied electric field for the 1.11-μm-thick film. The data were fit using Line-Profile Analysis Software (LIPRAS) [40]. An asymmetric Pearson VII function was applied to the 002 and 200 reflections since it accounts for peak asymmetry due to the diffuse scattering from ferroelectric/ferroelastic domain walls [41]. An example of the 002/200 peaks and fitting profiles is shown in Fig. 1(d) for the 1.11-μm-thick film at $0{\cdot}E_c$. Note that the presence of asymmetry and diffuse scattering can introduce systematic error for peak-fitting parameters such as peak position.

From the peak fit, ν_{002} (the fraction of c-domains oriented in the direction normal to the film) was calculated from the integrated intensities using the following equation, as described elsewhere [42], [43]:

$$\nu_{002} = \frac{\frac{I_{002}}{I'_{002}}}{\frac{I_{002}}{I'_{002}} + 2\frac{I_{200}}{I'_{200}}}. \tag{2}$$

The term I_{hkl} represents the integrated intensity of the hkl reflection determined using the unconvoluted half of the peak fit as described elsewhere [29]. I'_{hkl} represents the reference intensity from the powder diffraction file ($I'_{002} = 109$ and $I'_{200} = 249$) [44]. The error for ν_{002} was calculated using an error propagation method that accounts for the integrated intensity error generated from peak fitting using LIPRAS. The fraction of ferroelastic domain reorientation (η_{002}) was assessed using the following equation:

$$\eta_{002} = \nu_{002} - \nu_{002}^{0\text{field}}. \tag{3}$$

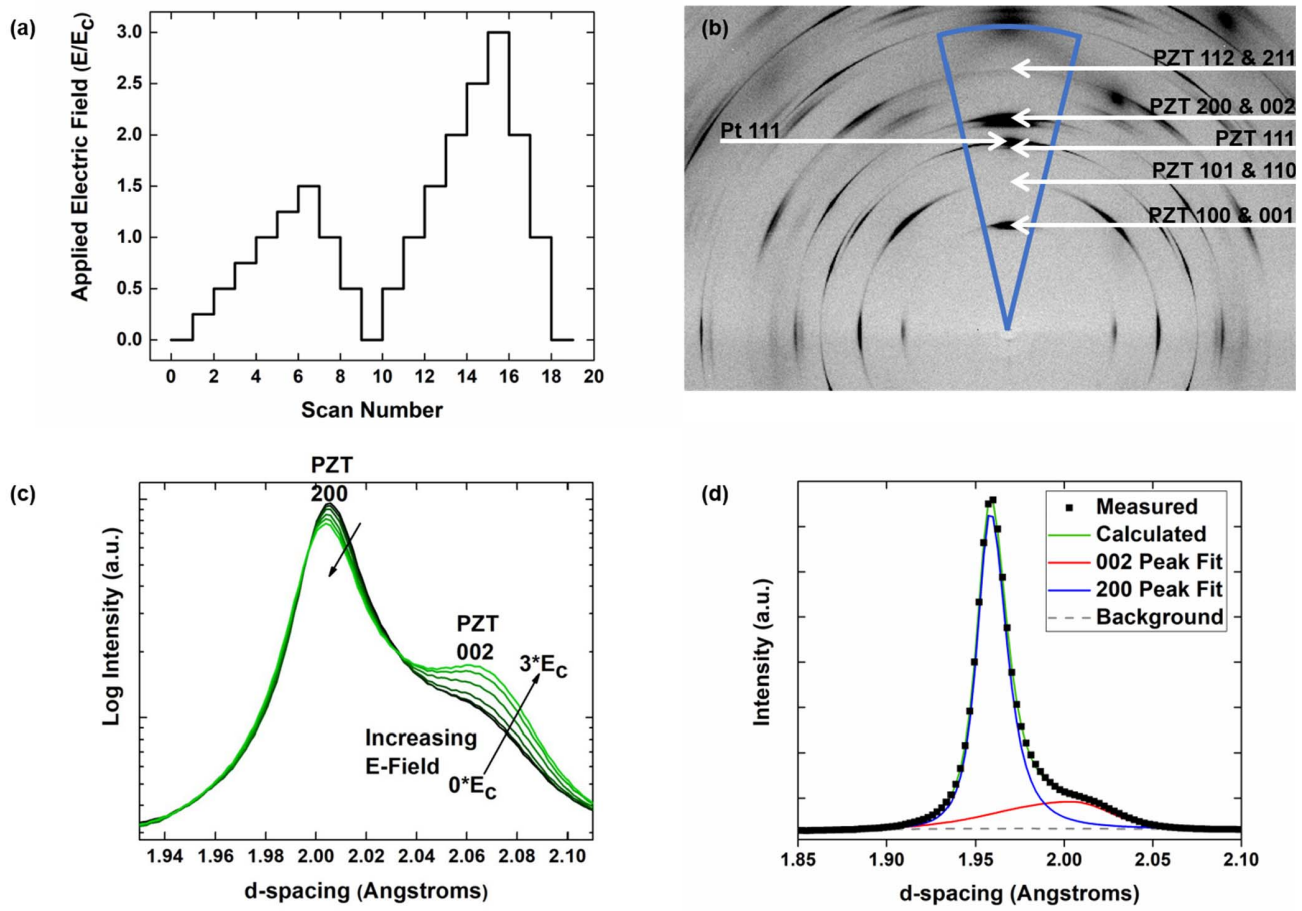

Fig. 1. (a) Schematic of the applied electric field cycles during the *in situ* XRD study. (b) 2-D diffraction image of the PZT 30/70 thin film with labeled reflections. (c) Example of the changes in peak intensity during application of electric field for the 1.11-μm PZT film. (d) Asymmetric Pearson VII fits of the 002 and 200 reflections of the 1.11-μm PZT film at $0{\cdot}E_C$.

The d-spacings of the 002 and 200 reflections (d_{002} and d_{200}, respectively) were used to calculate the strain (ε) induced by the electric field. The calculated pattern, background, and peak position generated from peak fitting using LIPRAS were used to determine the full-width at half-maximum (FWHM) of each reflection. For example, the FWHM of the 002 is determined to be two times the 2θ distance between the central peak position and the right-hand side of the peak (at a higher d-spacing) at the intensity value that is half the peak height. This calculation of the FWHM minimizes the error associated with the strong peak asymmetry associated with the diffuse scattering.

To study the lattice strain at high temperatures, a PANalytical Empyrean X'Pert3 MRD laboratory diffractometer with CuK_α radiation, a four-circle goniometer, and a PIXcel 3-D detector were used as a scanning line detector to measure diffraction patterns at 500 °C for wide 2θ ranges (10°–100°). The XRD pattern was collected at a slow scan rate of 0.72°/min.

Dielectric Rayleigh analysis was conducted on both clamped and released films at frequencies ranging from 50 Hz to 4 kHz with applied ac electric fields up to $0.5{\cdot}E_c$. The samples were subjected to annealing at 400 °C for 30 min and aging for 24 h prior to the Rayleigh measurements. Subsequently, the samples were poled at $3{\cdot}E_c$ for 15 min prior to additional Rayleigh measurements. A correction was used to account for the presence of a low dielectric permittivity seed layer electrically in series with the film [21].

C. Relative Permittivity Deconstruction

The combined electrical and structural data sets allow the possibility of separating the various contributions to the relative permittivity, assuming that each of the components is additive within the Rayleigh regime and that cross-coupling between the various terms can be neglected, as a first approximation. To do so, the intrinsic relative permittivity values ($\varepsilon_{r,\text{intrinsic}}$) were calculated using the following equation which accounts for the inherent dielectric anisotropy of a tetragonal PZT film:

$$\varepsilon_{r,\text{intrinsic}} = (1 - \nu_{002}) * \chi_{11} + \nu_{002} * \chi_{33}. \tag{4}$$

In (4), ν_{002} is the volume fraction of c-domains determined from diffraction measurements. The dielectric susceptibility values (χ_{11} and χ_{33}) can be used to approximate the relative permittivity values for a-domains and c-domains, respectively, since the relative permittivity values are much greater than 1. This assumption is based on the relationship between the relative permittivity and dielectric susceptibility ($\chi = \varepsilon_r - 1$). χ_{11} and χ_{33} are the free dielectric susceptibility (~230 and ~127,

respectively) determined by Haun *et al.* [45] for bulk PZT 30/70 at 25 °C. It is important to note that this calculation assumes a free system (fully released film). Because the films in this study are either in a clamped state or 75% released state, this approximation will overestimate the contributions from the intrinsic relative permittivity.

The reversible, extrinsic contributions to the relative permittivity ($\varepsilon_{r,\text{extrinsic}}^{\text{reversible}}$) were calculated from the following equation. The following equation assumes that $\varepsilon_{\text{initial}}$ is made up of intrinsic and reversible extrinsic contributions, which are additive within the Rayleigh regime:

$$\varepsilon_{r,\text{extrinsic}}^{\text{reversible}} = \varepsilon_{\text{initial}} - \varepsilon_{r,\text{intrinsic}}. \tag{5}$$

The irreversible, extrinsic contributions to the relative permittivity ($\varepsilon_{r,\text{extrinsic}}^{\text{irreversible}}$) was determined using the irreversible Rayleigh coefficient, α_ε, measured at 50 Hz and ac field of $0.5{\cdot}E_c$ as shown in (6). Note that the Rayleigh parameters $\varepsilon_{\text{initial}}$ and α_ε measured at 50 Hz were used in (5) and (6), respectively, to represent the relative permittivity deconstruction with maximum extrinsic contributions measured in this study

$$\varepsilon_{r,\text{extrinsic}}^{\text{irreversible}} = \alpha_\varepsilon E_0. \tag{6}$$

For comparison, $\varepsilon_{r,\text{extrinsic}}^{\text{irreversible}}$ was also calculated by subtracting $\varepsilon_{\text{initial}}$ from the measured ε_r (measured at 50 Hz and ac field of $0.5{\cdot}E_c$), as shown in the following equation:

$$\varepsilon_{r,\text{extrinsic}}^{\text{irreversible}} = \varepsilon_r^{\text{measured}} - \varepsilon_{\text{initial}}. \tag{7}$$

The comparison in the calculations for $\varepsilon_{r,\text{extrinsic}}^{\text{irreversible}}$ can be found in Supplemental Tables I and II for clamped films (unpoled versus poled) and released films (unpoled versus poled), respectively. In general, negligible differences in $\varepsilon_{r,\text{extrinsic}}^{\text{irreversible}}$ calculated using (6) versus (7) were found for films that were poled, regardless of their released state. For example, $\varepsilon_{r,\text{extrinsic}}^{\text{irreversible}}$ calculated using (6) and (7) for a poled, clamped film with a thickness of 1.11 μm was 338 $\pm$ 6 and 338 $\pm$ 2, respectively. However, differences as large as 20% in $\varepsilon_{r,\text{extrinsic}}^{\text{irreversible}}$ calculated using (6) versus (7) are shown for unpoled films. These differences are likely due to error associated with the linear extrapolation of the Rayleigh analysis in unpoled films.

The Rayleigh coefficients $\varepsilon_{\text{initial}}$ and α_ε are frequency dependent within the measurement range of 50 Hz–4 kHz. That is, smaller values are observed at higher frequencies wherein domain wall motion contributions are suppressed presumably due to slow-moving walls. Therefore, to maximize the domain wall motion contributions in the relative permittivity deconstruction, $\varepsilon_{\text{initial}}$ and α_ε determined at 50 Hz (the lowest frequency used in the Rayleigh analysis) were used to calculate $\varepsilon_{r,\text{extrinsic}}^{\text{reversible}}$ and $\varepsilon_{r,\text{extrinsic}}^{\text{irreversible}}$, respectively.

III. Results and Discussion

A. Thickness Dependence of the Domain State

The volume fraction of *c*-domains (ν_{002}) and the change in this volume fraction relative to the unpoled state (η_{002}) are shown in Fig. 2 for clamped, 2% Nb-doped PZT 30/70 thin films of thicknesses 0.27, 0.56, and 1.11 μm. Most of the clamped films underwent two electric field cycles: the first being a low-amplitude cycle and the second being a high-amplitude cycle. The ramp down of cycle 1 and the ramp up of cycle 2 often overlapped. For simplification, where the data overlap, only a single cycle is shown. Note that the 75% released 1.11-μm-thick film exceeded a threshold current of 1×10^{-4} A/cm^2 at electric fields exceeding $2{\cdot}E_c$. Therefore, the data for the released 1.11-μm film above $1.5{\cdot}E_c$ were removed.

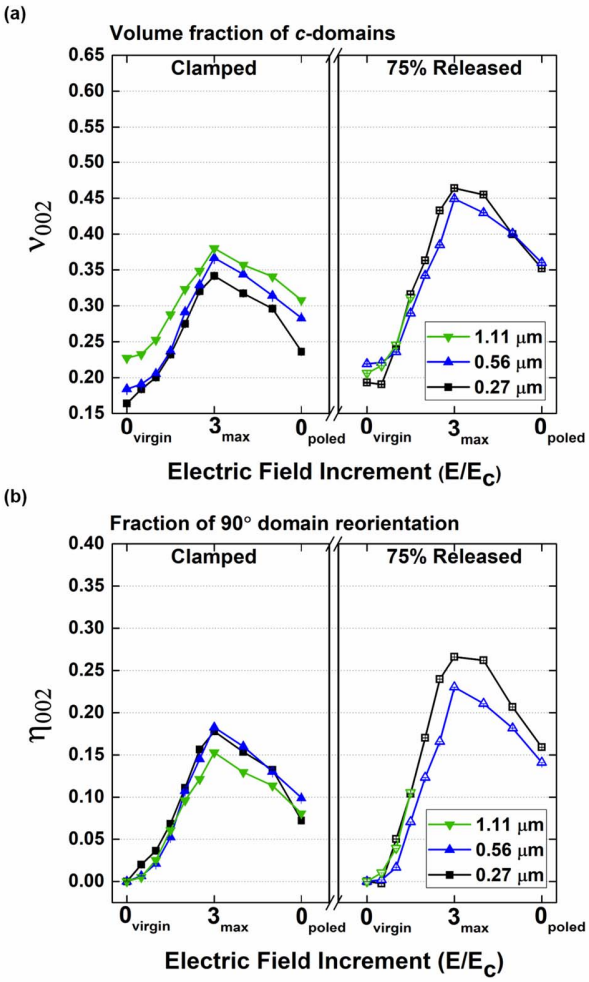

Fig. 2. (a) Volume fraction of *c*-domains (ν_{002}◁ as a function of applied electric field is shown for 2% Nb-doped PZT 30/70 thin films of thicknesses 0.27, 0.56, and 1.11 μm in the clamped state and in the released state. The 75% released 1.11-μm-thick film exceeded a threshold current of 1×10^{-4} A/cm^2 at electric fields exceeding $2{\cdot}E_c$. Therefore, the data for the released 1.11-μm film above $1.5{\cdot}E_c$ were removed. (b) Fraction of 90° domain reorientation (η_{002}◁ as a function of applied electric field is also shown for the clamped state and the released state.

From Fig. 2, in the clamped virgin state, ν_{002} is thickness dependent and ranges between 0.23 (for the 1.11-μm film) and 0.16 (for the 0.27-μm film), which are comparable to those in the literature for similar compositions, thicknesses, and processing methods [21], [29]. This thickness dependence of ν_{002} is maintained after poling at $3{\cdot}E_c$. That is, thicker clamped films have a high-volume fraction of *c*-domains than thinner clamped films in the initial state, during field application, and after release of field.

The thickness dependence of ν_{002} develops during processing of the films [18]. For example, Supplemental Fig. 1 shows the evolution of the normalized ν_{001} during layer-by-layer processing of a ~0.5-μm-thick sample, in which ν_{001} increases with each additional crystallized layer. Presumably, this evolution in the domain state is related to both the stress state of the film upon cooling below the Curie temperature, T_c, and the defect chemistry of the interfaces.

A second point of note from Fig. 2(a) is that upon 75% release from the substrate (with an anneal above T_c), ν_{002} values converge to ~0.2 ± 0.01 for all films prior to application of an electric field. It is proposed that after a high temperature anneal, a redistribution of the domain state occurred. The release relieves local stress at the film–substrate interface and reduces the bending rigidity of the structure. As a result, the released portions of the film experienced a different stress compared with its clamped counterpart upon cooling below T_c. Annealing above T_c allows redistribution of the domain state in the released films, whereas when the annealing was not performed, no change in the volume fraction of c-domains was observed after films were released from the substrate [28].

Third, when an electric field is applied, a much larger volume fraction of c-domains is achieved for all film thicknesses in released films relative to clamped ones. This is particularly true at $3{\cdot}E_c$. Above $1.5{\cdot}E_c$, the diaphragms tear due to the high piezoelectric strains and release geometry [29]. After tearing, portions of the film are free to deflect vertically to relieve in-plane tensile stress, creating cantilever-like regions. A SEM image of these cantilever-like regions can be seen in Fig. 1 of an article by Denis *et al.* [21]. This state is referred to as global release. After global release, both the 0.27- and 0.56-μm-thick films show nearly 50% c-domain fractions at $3{\cdot}E_c$. ν_{002} is comparable for all thicknesses even after poling.

Fig. 2(b) shows electric field-induced changes in η_{002} for all film thicknesses in the clamped state and 75% released state. In the clamped state, each film experiences similar levels of ferroelastic domain reorientation during poling and similar back-switching regardless of film thickness (i.e., the relaxation of reoriented domains back to a remanent state as the electric field decreases to zero). These results suggest that substrate clamping acts as the dominant restoring force for back switching in clamped films. In the clamped state, η_{002} is ~0.18 at $3{\cdot}E_c$ which is almost four times larger than what has been previously reported for ~1.9-μm-thick clamped 1% Mn-doped PZT 30/70 films [29]. The enhanced domain reorientation in the 2% Nb-doped PZT films of this study is consistent with softening of the electromechanical response. Additionally, after release, all film thicknesses have comparable electric field-induced changes in η_{002}, as shown in Fig. 2(b). As expected, more domain reorientation is observed in the released films than in the clamped ones [29].

B. Thickness Dependence of Residual Stress

In the clamped state, the thinnest 0.27-μm film has the smallest out-of-plane d-spacing for a- and c-domains, d_{200} and d_{002}, respectively, as shown in Fig. 3. The domains present in an as-processed, clamped film are under in-plane tensile

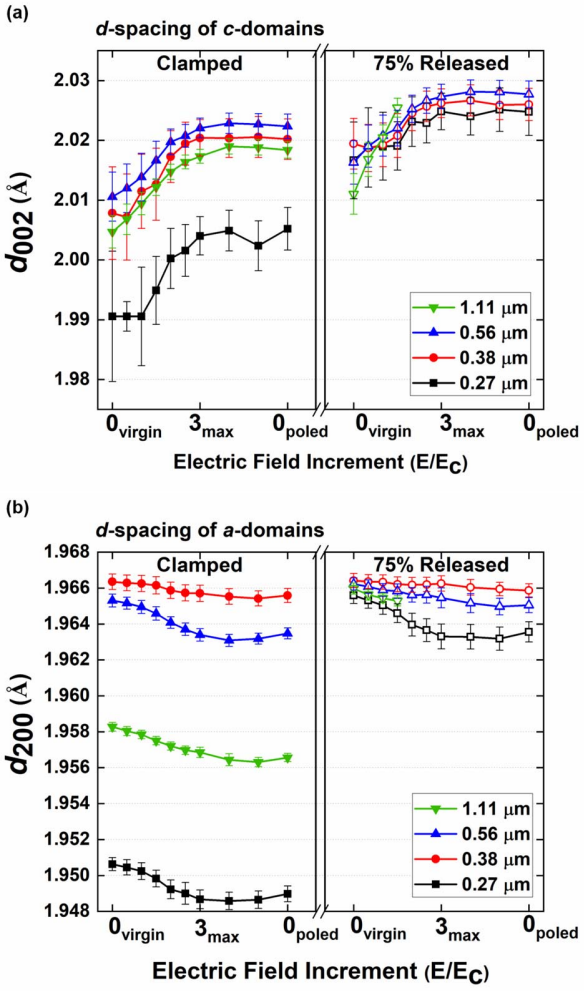

Fig. 3. d-spacing for the (a) 002 and (b) 200 reflections (d_{002} and d_{200}, respectively) as a function of applied electric field increment for 2% Nb-doped PZT 30/70 thin films of thicknesses 0.27, 0.38, 0.56, and 1.11 μm in the clamped state and the 75% released state is shown.

stress due to a variety of factors including strain related to defect concentrations and thermal strain formed due to the thermal expansion coefficient mismatch between the film and the substrate.

Thinner films experience a greater in-plane tensile stress that develops upon cooling below T_c which contributes to smaller out-of-plane d spacings for the 0.27-μm film [15]. Additionally, Supplemental Fig. 2 shows a thickness dependence in the d spacings that persists above T_c, suggesting that a greater concentration of defects in thinner films also contributes to smaller d spacings for the 0.27-μm film. It is assumed that thinner films have a greater population of nonstoichiometric defects since regions of lead deficiency make up an overall greater volume of the film itself. These defects form at the surface of the film due to lead volatilization during crystallization and at the film–substrate interface due to lead loss to the bottom electrode during crystallization. The d spacings were determined from the peak fit of the 002 cubic reflection which was relatively symmetric at 500 °C. Thus, the thickness dependence in the out-of-plane lattice spacings for clamped films is attributed to both a larger in-plane tensile stress and

a higher concentration of defects in thinner films. This is consistent with the data of Berfield *et al.* [5] suggesting that chemical solution-derived PZT films ~200 nm in thickness have higher in-plane tensile stresses than thicker films when grown on Pt-coated Si substrates. Thus, thin PZT films that have higher in-plane tensile stress should experience a larger change in stress when released from the substrate compared with thicker films

Interestingly, d_{200} does not monotonically increase with increasing thickness from 0.27 to 1.11 μm, as shown in Fig. 3(b). The films reported in this study have smaller out-of-plane lattice parameters compared with their bulk counterpart due to the in-plane tensile stress that PZT experiences when processed on an Si substrate. If the in-plane tensile stress decreases with increasing film thickness, as suggested elsewhere [18], it should be reflected in a gradual increase in d_{200}. Additionally, at temperatures above T_c, d spacing is also observed to increase with increasing thickness for these films. However, at room temperature, Fig. 3(b) shows that the d_{200} sharply increases as film thickness increases from 0.27 to 0.38 μm and then decreases as film thickness increases further from 0.38 to 1.11 μm. Reasons for this are unclear, but these changes are consistent with a reported decrease in the reversible Rayleigh coefficient with increasing thickness for films >0.38 μm [21]. This suggests that competing factors may influence the thickness dependence of d_{200}.

For both clamped and released films, d_{002} increases with increasing applied electric field as shown in Fig. 3(a). A complete data set of d_{002} and d_{200} as a function of applied field for all film thicknesses is shown in Supplemental Fig. 3, along with the values of the unpoled, bulk ceramic counterparts of similar compositions [46]. The field-induced changes in d_{002} are substantially too large to be due only to the intrinsic piezoelectric response, as the required $d_{33,f}$ on increasing field would need to exceed ~250 pm/V in the clamped films. Moreover, the d_{002} values do not recover when the field is removed.

Under applied electric fields, rewriting the domain state will change both the residual stress state of the film and the domain size. For example, d_{002} increases with increasing applied electric fields, whereas d_{200} decreases. It is notable that the increase in d_{002} is accompanied by a reduction in the FWHM of the 002 peak, while the FWHM of the 200 peak increases on poling, as shown in Fig. 4(a) for a clamped 1.11-μm-thick film. This suggests that the c-domains coarsen on poling. Fig. 5 shows schematically the movement of 90° and 180° domain walls upon poling coupled with the coarsening of c-domains oriented parallel to the applied electric field (highlighted in gray). In this schematic (not to scale), a larger increase in the volume fraction of c-domains upon application of electric field is shown for released films (right) compared with clamped films (middle).

As the c-domains coarsen, they begin to approach the d-spacing values for bulk ceramics of the same composition. This is presumably the cause of the irreversible strains in d_{002} on poling. After ferroelastic switching occurs, unswitched a-domains are placed under further in-plane tension by neighboring c-domains reoriented by the applied electric field.

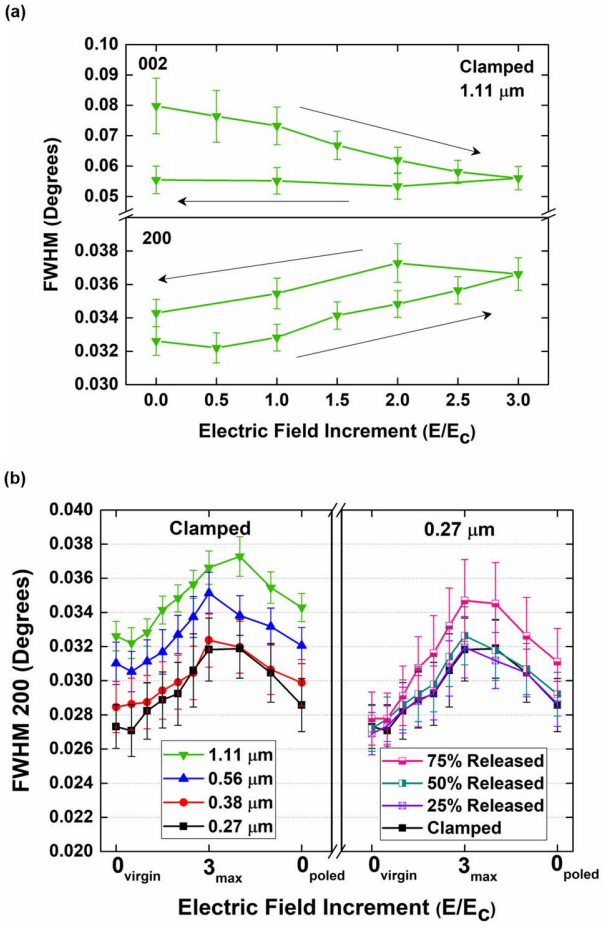

Fig. 4. (a) FWHM for the 002 and 200 reflections as a function of applied electric field is plotted for 2% Nb-doped PZT 30/70 thin films of thickness 1.11 μm. (b) FWHM for the 200 reflection as a function of applied electric field is plotted for clamped films of thicknesses ranging from 0.27 to 1.11 μm (left); and FWHM for the 200 reflection as a function of applied electric field is plotted for the 0.27-μm film for all released states (right).

As a result, d_{200} decreases. This is observed for tetragonal PZT thin films as an anisotropic electric field-induced change in the out-of-plane d-spacings [47]. Additionally, the FWHM of the a-domains increases irreversibly upon application of electric field, presumably due to the microstrain that develops during irreversible 90° switching. Since some 90° domain reorientations are not recoverable, the residual strain associated with ferroelastic switching results in an irreversible change in d_{002}, d_{200}, FWHM of 002, and FWHM of 200.

In general, the FWHM of the 200 is smaller than that of the 002, as shown in Fig. 4(a) for the 1.11-μm-thick film (and was true for all film thicknesses). Preliminary Williamson Hall analysis (not corrected for instrumental broadening) suggests that tetragonal PZT films under in-plane tensile stress favors larger a-domain crystallites and a greater volume fraction of a-domains, as shown in Supplemental Fig. 4 and represented schematically in Fig. 5. In-plane residual stress and local stresses formed during electrical actuation may induce variable a-domain crystallite sizes, thereby contributing to the larger FWHM of the 200 peak. Additionally, the FWHM of 200 increases as film thickness increases, as shown in Fig. 4(b). Moreover, the thickness dependence in the FWHM of 200 is maintained even after poling.

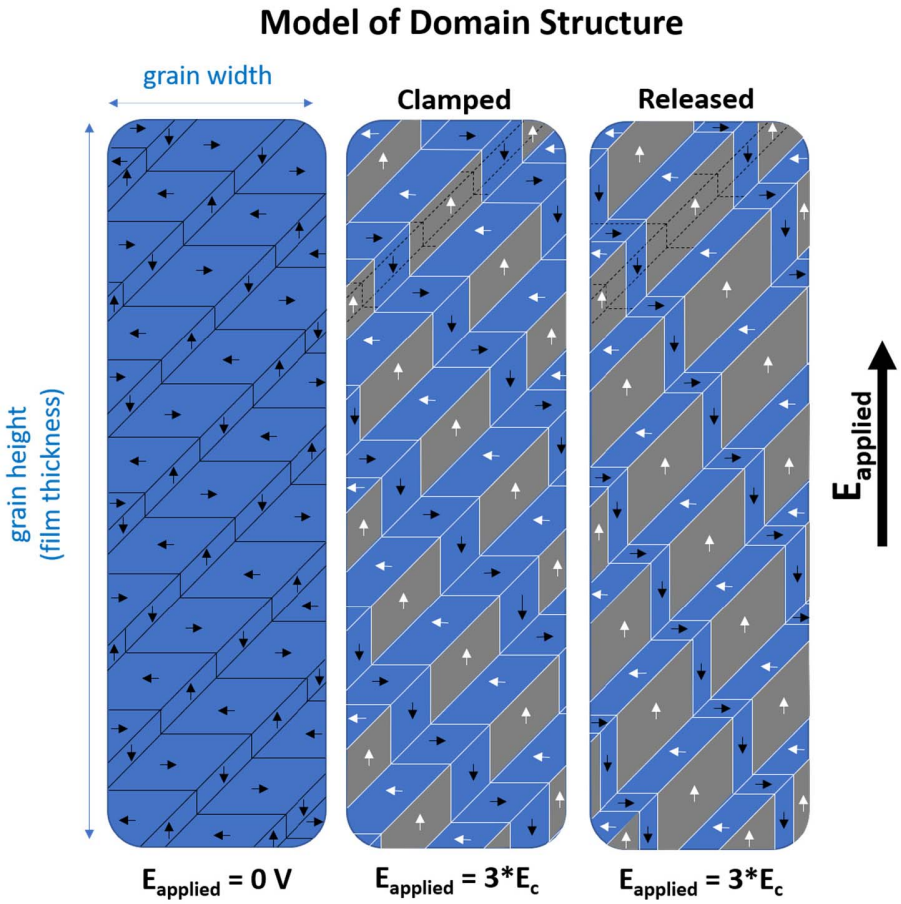

Fig. 5. Model of the domain structure within one grain before (left) and after (middle and right) poling to $3{\cdot}E_c$ for a clamped grain (middle) and released grain (right). In general, the volume fraction of *c*-domains increases, and the *c*-domains coarsen upon application of electric field. This increase is greater for released films compared with clamped films, shown by the large *c*-domain crystallites in the released grain. (Note: Schematic is exaggerated for clarity.)

Releasing from the substrate followed by annealing above T_c (∼450 °C) relieves the in-plane tensile stress of the film, resulting in an increase in d-spacing, as shown in Fig. 3. The largest increase in both d_{200} and d_{002} occurs for the 0.27-μm film (0.76% and 1.32% increase, respectively). Upon release, the d_{200} and d_{002} converge to ∼1.966 ± 0.001 and ∼2.015 ± 0.01 Å, respectively, for all film thicknesses in the virgin state. The annealing temperature is too low to expect significant changes in Pb stoichiometry, so the change in d spacing is attributed to the strain relaxation associated with different mechanical boundary conditions once the film is globally released. These results confirm that 0.27-μm film experiences a greater strain relaxation upon release and is likely linked to a larger increase in the irreversible Rayleigh response upon release [21].

At applied electric fields of $3{\cdot}E_c$, the FWHM of 200 is enhanced postrelease by ∼9% for the 0.27-μm-thick film, as shown in Fig. 4(b). Small differences in the FWHM as a function of release state develop after globally releasing the film from the substrate (applied electric fields ≥ $1.5{\cdot}E_c$ for which tearing of the diaphragms occurs). Therefore, the increase in the FWHM upon release may be due to electric-field-induced nonuniformities in microstrain and/or crystallite size. Improvements in peak-fitting quality of low-intensity thin films are needed to confirm that these differences are statistically significant.

C. Rayleigh Poling Study

Previous studies have shown that Rayleigh parameters α_ε and $\varepsilon_{\text{initial}}$ have a complicated thickness dependence that is influenced by the domain state of the film and changes upon release [21]. Complementary Rayleigh analysis was conducted to investigate whether the thickness dependence of α_ε and $\varepsilon_{\text{initial}}$ changes upon poling. Dispersion curves of the Rayleigh parameter α_ε as a function of frequency are shown in Fig. 6(a) and (b) for unpoled and poled PZT films in the clamped state, respectively. In general, α_ε decreases upon poling, presumably due to the decrease in domain wall density associated with the coarsening of *c*-domains inferred from the smaller FWHM of the 002 reflection. Small (<9%) thickness-independent changes in α_ε occur upon poling for clamped films.

Upon 75% release from the substrate, α_ε increases for all film thicknesses, as shown in Fig. 6(c). Moreover, after poling, the change in α_ε for the 75% released film is more than double than that for the clamped film. The changes in α_ε are the

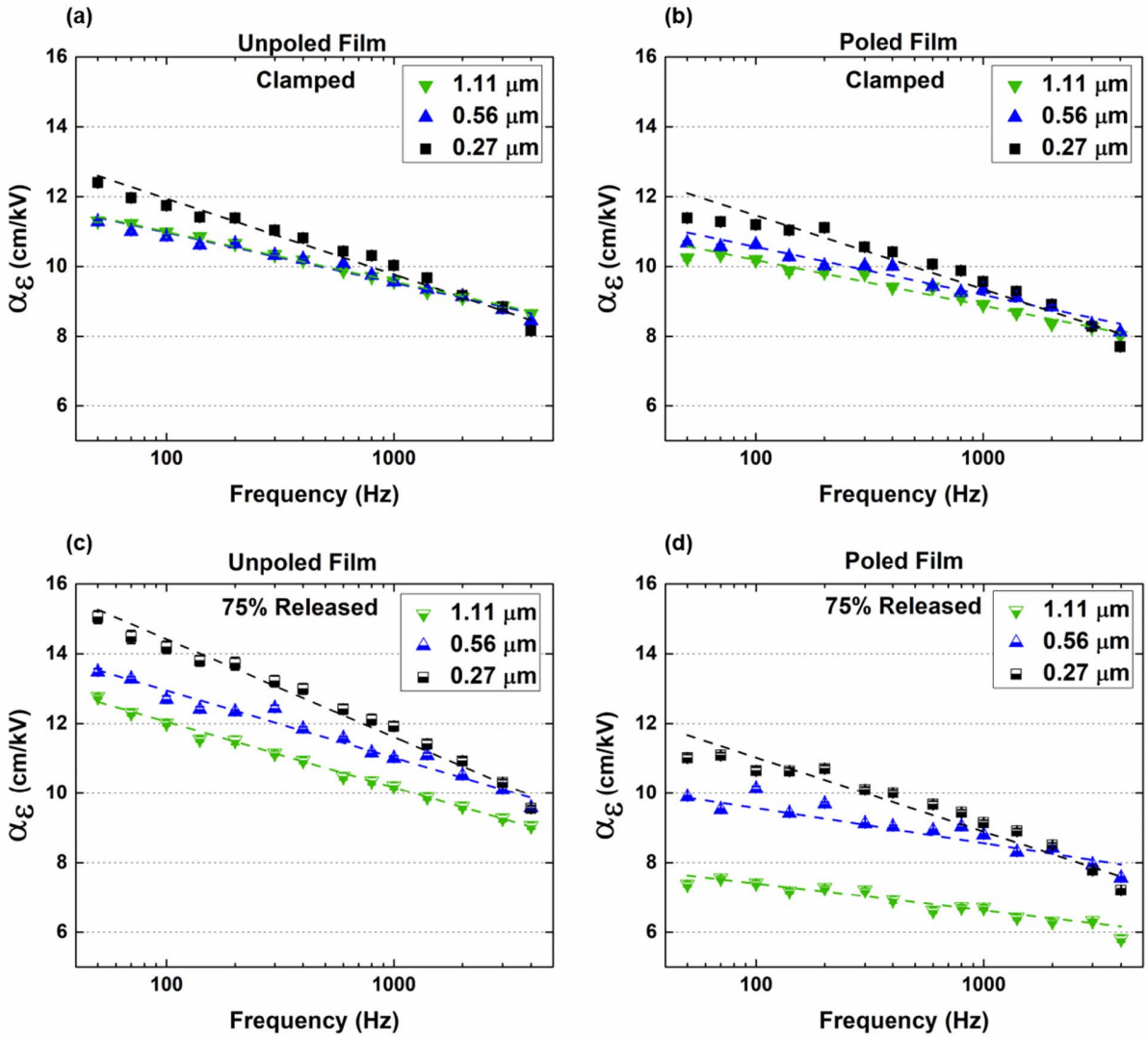

Fig. 6. Frequency dispersion of the Rayleigh parameter α_ε as a function of film thickness ranging from 0.27 to 1.11 μm for 2% Nb-doped PZT 30/70 thin films in the clamped state for (a) unpoled and (b) poled films and in the 75% released state for (c) unpoled and (d) poled films.

largest at low frequencies, confirming observations reported elsewhere that substrate clamping has a greater influence on slower, irreversibly moving, domain walls [21]. Finally, since releasing the film from the substrate enhances ferroelastic domain reorientation, it can be assumed that the greater change in α_ε for released films is due to a greater decrease in domain wall density resulting from c-domain coarsening upon poling.

Dispersion curves of $\varepsilon_{\text{initial}}$ are shown in Fig. 7 for unpoled (a) and poled (b) clamped PZT films. $\varepsilon_{\text{initial}}$ decreases upon poling due to the increases in volume fraction of c-domains coupled with a decrease in domain wall density due to coarsening of the c-domains. The thickness dependence of $\varepsilon_{\text{initial}}$ increases after poling, with a three times larger change in $\varepsilon_{\text{initial}}$ for the 1.11-μm film ($\sim$16%) compared with the 0.27-μm film ($\sim$5%). This thickness-dependent change in $\varepsilon_{\text{initial}}$ is not due to differences in the ferroelastic domain reorientation, since η_{002} is not thickness dependent (see Fig. 2). Additionally, the thickness-dependent change in $\varepsilon_{\text{initial}}$ is not intrinsically driven since there is no change in the thickness dependence of ν_{002}. The large Rayleigh coefficients (α_ε and $\varepsilon_{\text{initial}}$) reported for the clamped, unpoled 0.27-μm film relative to thicker films may be due in part to a greater domain wall density present in the film. The thinnest 0.27-μm film presumably has the largest domain wall density due to its small crystallite size, as suggested by the preliminary Williamson Hall analysis in Supplemental Fig. 4 [48].

The *in situ* XRD analysis can be used to determine whether thickness-dependent changes in $\varepsilon_{\text{initial}}$ upon poling is driven by intrinsic or reversible extrinsic contributions to the permittivity. Estimated values for $\varepsilon_{r,\text{intrinsic}}$ are plotted as a function of film thickness for unpoled and poled films in both the clamped and 75% released states, as shown in the lower portion of Fig. 8. For a clamped unpoled film, $\varepsilon_{r,\text{intrinsic}}$ decreases as thickness increases, which coincides with the thickness-dependent trends for ν_{002}. However, upon 75% release from the substrate, the thickness dependence in $\varepsilon_{r,\text{intrinsic}}$ is reduced. Therefore, the thickness dependence in $\varepsilon_{\text{initial}}$ for the unpoled, 75% released state is due predominantly to a thickness dependence in the

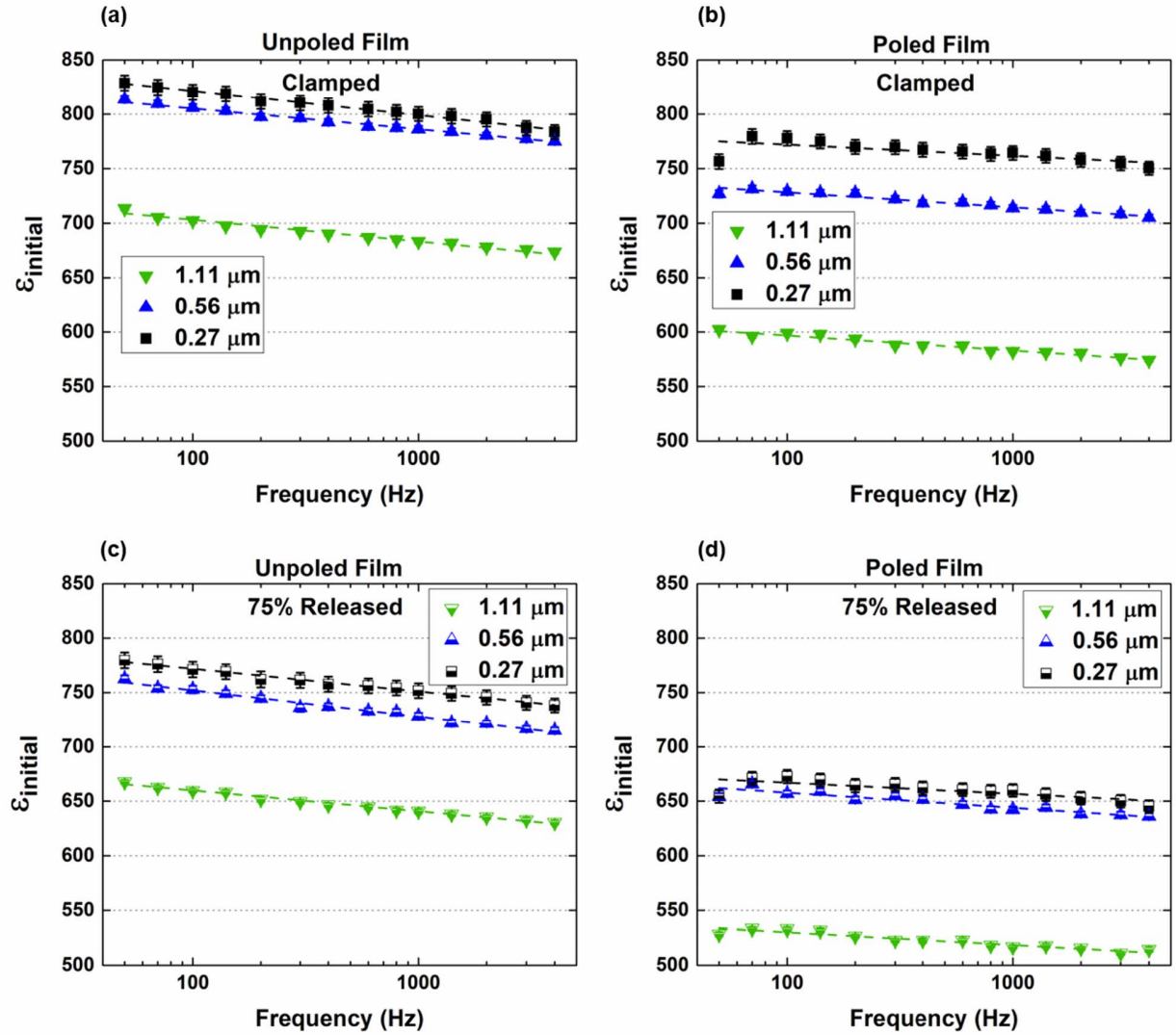

Fig. 7. Frequency dispersion of the Rayleigh parameter $\varepsilon_{\text{initial}}$ as a function of film thickness ranging from 0.27 to 1.11 μm for 2% Nb-doped PZT 30/70 thin films in the clamped state for (a) unpoled and (b) poled films and in the 75% released state for (c) unpoled and (d) poled films.

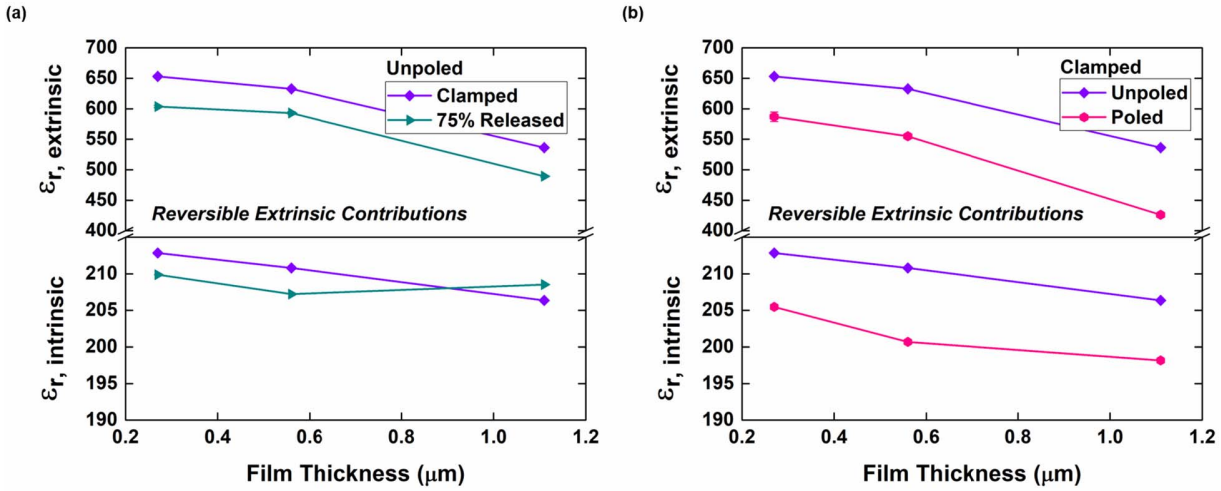

Fig. 8. Intrinsic ($\varepsilon_{r,\text{intrinsic}}$) and reversible extrinsic ($\varepsilon_{r,\text{extrinsic}}^{\text{reversible}}$) contributions to the permittivity as a function of film thickness ranging from 0.27 to 1.11 μm for 2% Nb-doped PZT 30/70 thin films in the (a) clamped state and 75% released state for unpoled and in the (b) clamped state for unpoled and poled films.

reversible extrinsic contribution to the relative permittivity ($\varepsilon_{r,\text{extrinsic}}^{\text{reversible}}$). Upon release, $\varepsilon_{\text{initial}}$ decreases by ~6% for all film thicknesses, as shown in Fig. 8(c), which is mainly related to a shift from reversible to irreversible domain wall contributions to the relative permittivity [21]. Phenomenological calculations suggest that the $\varepsilon_{r,\text{extrinsic}}^{\text{reversible}}$ decreases upon

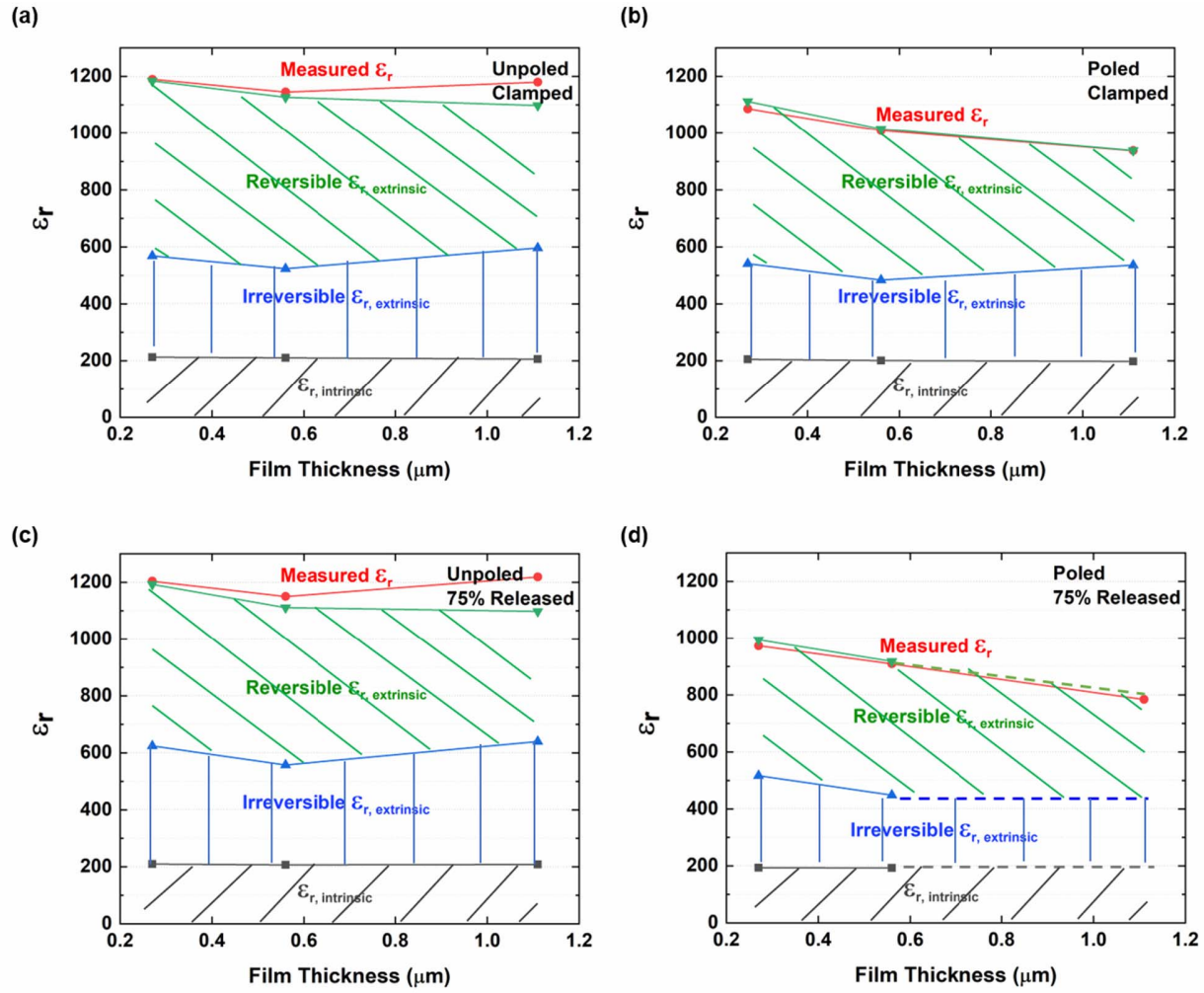

Fig. 9. Intrinsic ($\varepsilon_{r,\text{intrinsic}}$), reversible, and irreversible extrinsic ($\varepsilon_{r,\text{extrinsic}}^{\text{reversible}}$ and $\varepsilon_{r,\text{extrinsic}}^{\text{irreversible}}$) contributions to the permittivity as a function of film thickness ranging from 0.27 to 1.11 μm for 2% Nb-doped PZT 30/70 thin films in the clamped state for (a) unpoled and (b) poled films and in the 75% released state for (c) unpoled and (d) poled films. Note that the gray square data points represent $\varepsilon_{r,\text{intrinsic}}$, the blue triangle data points represent $\varepsilon_{r,\text{intrinsic}} + \varepsilon_{r,\text{extrinsic}}^{\text{irreversible}}$, the green inverted triangle data points represent $\varepsilon_{r,\text{intrinsic}} + \varepsilon_{r,\text{extrinsic}}^{\text{irreversible}} + \varepsilon_{r,\text{extrinsic}}^{\text{reversible}}$, and the red circle data points represent the relative permittivity measured at 50 Hz and ac field of $0.5 \cdot E_C$.

release for all film thicknesses, driving the overall decrease in $\varepsilon_{\text{initial}}$.

For clamped films, $\varepsilon_{r,\text{intrinsic}}$ decreases upon poling, with a comparable decrease for all film thicknesses (3.4% decrease for 0.27 μm versus 4.0% decrease for 1.11 μm), as shown in the lower portion of Fig. 8(b). Therefore, it is confirmed that the thickness-dependent change in $\varepsilon_{\text{initial}}$ upon poling for a clamped film is not due to intrinsic changes. In general, $\varepsilon_{r,\text{extrinsic}}^{\text{reversible}}$ decreases as thickness increases regardless of the released state for both unpoled and poled samples, as shown in the upper portion of Fig. 8(a) and (b). These results suggest that substrate clamping creates deep potential wells in the potential energy landscape in which reversible motion of domain walls is preferred, consistent with studies by Griggio *et al.* [14]. Additionally, it is probable that domain wall motion in thinner films exhibits more reversible motion compared with thicker films, since a greater fraction of domain walls in thinner films are subject to clamping effects at the film–substrate interface. For clamped films, the decrease in $\varepsilon_{r,\text{extrinsic}}^{\text{reversible}}$ upon poling in the thicker 1.11-μm film is double than that for the thinner 0.27-μm film (20% decrease versus 10% decrease, respectively). Therefore, the thickness-dependent change in $\varepsilon_{\text{initial}}$ upon poling of a clamped film is primarily due to extrinsic contributions. It is proposed that thicker films, which have reduced in-plane tensile stress and defect concentrations, experience a greater coarsening of *c*-domains upon poling. As a result, thicker films have smaller domain wall densities in the poled state, resulting in a greater decrease in both $\varepsilon_{r,\text{extrinsic}}^{\text{reversible}}$ and $\varepsilon_{\text{initial}}$ upon poling.

For the first time, the deconstruction of the relative permittivity into its individual contributions was achieved by combining XRD and Rayleigh analysis. By using this technique, the values of the reversible extrinsic contribution are deconvoluted. Additionally, the reversible and irreversible extrinsic contributions can be directly compared with better understand the nature of the potential energy landscape of films for various mechanical and electrical boundaries conditions, e.g., clamped versus released and poled versus unpoled. It is assumed that

the intrinsic, reversible extrinsic, and irreversible extrinsic contributions are additive; strong coupling between reversible and irreversible mechanisms would lead to errors in the derived values. Thus, this approach is only valid for measurements taken within the Rayleigh regime in samples for which the Rayleigh law is valid.

The relative permittivity can be separated into three contributions: intrinsic, reversible extrinsic, and irreversible extrinsic contributions, as shown in Fig. 9. It was found that for these films, $\varepsilon_{r,\text{extrinsic}}^{\text{reversible}}$ makes up a majority of the relative permittivity (approximately 50%). As noted in the Fig. 9 caption, the individual contributions to the measured permittivity are assumed to be additive and are plotted to show the linear superposition of the contributions. As discussed above, it is assumed that the cross terms are negligible at low applied electric fields (within the Rayleigh regime: $E_{\text{applied}} \leq E_c$). It is also possible that properly accounting for clamping of the intrinsic relative permittivity would drop that contribution by roughly a factor of two, with the difference contributing to the reversible extrinsic permittivity. Differences between the measured relative permittivity (red circle data points) and the summation of the three contributions (green inverted triangle data points) may be due to the error associated with assuming the cross terms are negligible, the error associated with using released relative dielectric permittivity terms to calculate the intrinsic response, or errors associated with peak fitting.

IV. Conclusion

In situ high-resolution XRD was used to investigate the influence that substrate clamping and residual stress have on the thickness dependence of the volume fraction of c-domains and electric field-induced strain upon release. Tetragonal {001} $Pb_{0.99}(Zr_{0.3}Ti_{0.7})_{0.98}Nb_{0.02}O_3$ films were deposited using CSD with thicknesses ranging from 0.27 to 1.11 μm. The thickness dependence of ν_{002} is influenced by the concentration of defects in the films and the degree of residual stress formed upon cooling below T_c. This thickness dependence persists after poling and is alleviated upon release. The thickness dependence of ν_{002} can result in differences in the intrinsic contributions to reversible Rayleigh parameter, $\varepsilon_{\text{initial}}$. The thinnest 0.27-$\mu$m film has the smallest d-spacings for both a- and c-domains due to a greater in-plane tensile stress and a higher concentration of defects present in thinner films. In general, the electric field-induced change in d_{002} and d_{200} is irreversible due to factors such as irreversible coarsening of c-domains and irreversible 90° domain reorientation, both of which will change the local stress state of the film. Releasing the film from the substrate relieves residual stress, increases the FWHM of the 200 reflection, and enhances ferroelastic domain reorientation. Residual stress in a film indirectly affects the extent of reversible, extrinsic contributions to the relative permittivity. These results confirm that residual stress at the film–substrate interface creates a potential energy landscape with deep potential wells, such that reversible motion of domain walls is preferred.

The combination of XRD and Rayleigh analysis allows the relative dielectric permittivity to be decomposed into intrinsic, reversible extrinsic, and irreversible extrinsic contributions. It was found that at 50 Hz and at an applied field of $0.5 \cdot E_c$, the reversible motion of domain walls provides the largest contribution to the total dielectric permittivity in both clamped and released films for all the investigated films.

Acknowledgment

The technical assistance of Guy Jennings, Rick Spence, and Yang Ren at beamline 11-ID-C, Argonne National Laboratory, Lemont, IL, USA, is gratefully acknowledged.

References

[1] P. Muralt, "Ferroelectric thin films for micro-sensors and actuators: A review," *J. Micromech. Microeng.*, vol. 10, no. 2, pp. 136–146, Jun. 2000, doi: 10.1088/0960-1317/10/2/307.

[2] N. Setter *et al.*, "Ferroelectric thin films: Review of materials, properties, and applications," *J. Appl. Phys.*, vol. 100, no. 5, Sep. 2006, Art. no. 051606, doi: 10.1063/1.2336999.

[3] T. M. Shaw, S. Trolier-McKinstry, and P. C. McIntyre, "The properties of ferroelectric films at small dimensions," *Annu. Rev. Mater. Sci.*, vol. 30, no. 1, pp. 263–298, Aug. 2000, doi: 10.1146/annurev.matsci.30.1.263.

[4] J. F. Ihlefeld, D. T. Harris, R. Keech, J. L. Jones, J.-P. Maria, and S. Trolier-McKinstry, "Scaling effects in perovskite ferroelectrics: Fundamental limits and process-structure-property relations," *J. Amer. Ceram. Soc.*, vol. 99, no. 8, pp. 2537–2557, Aug. 2016, doi: 10.1111/jace.14387.

[5] T. A. Berfield, R. J. Ong, D. A. Payne, and N. R. Sottos, "Residual stress effects on piezoelectric response of sol-gel derived lead zirconate titanate thin films," *J. Appl. Phys.*, vol. 101, no. 2, Jan. 2007, Art. no. 024102, doi: 10.1063/1.2422778.

[6] G. A. C. M. Spierings, G. J. M. Dormans, W. G. J. Moors, M. J. E. Ulenaers, and P. K. Larsen, "Stresses in Pt/Pb(zr,Ti)O_3/Pt thin-film stacks for integrated ferroelectric capacitors," *J. Appl. Phys.*, vol. 78, no. 3, pp. 1926–1933, Aug. 1995, doi: 10.1063/1.360230.

[7] D. G. Schlom, L.-Q. Chen, C.-B. Eom, K. M. Rabe, S. K. Streiffer, and J.-M. Triscone, "Strain tuning of ferroelectric thin films," *Annu. Rev. Mater. Res.*, vol. 37, no. 1, pp. 589–626, Aug. 2007, doi: 10.1146/annurev.matsci.37.061206.113016.

[8] B. A. Tuttle *et al.*, "Chemically prepared Pb(Zr, Ti)O_3 thin films: The effects of orientation and stress," in *Proc. 8th IEEE Int. Symp. Appl. Ferroelectr. (ISAF)*, Aug. 1992, pp. 344–348, doi: 10.1109/ISAF.1992.300703.

[9] J. S. Speck, A. C. Daykin, A. Seifert, A. E. Romanov, and W. Pompe, "Domain configurations due to multiple misfit relaxation mechanisms in epitaxial ferroelectric thin films. III. Interfacial defects and domain misorientations," *J. Appl. Phys.*, vol. 78, no. 3, pp. 1696–1706, Aug. 1995, doi: 10.1063/1.360267.

[10] K. Lee and S. Baik, "Ferroelastic domain structure and switching in epitaxial ferroelectric thin films," *Annu. Rev. Mater. Res.*, vol. 36, no. 1, pp. 81–116, Aug. 2006, doi: 10.1146/annurev.matsci.36.090804.094613.

[11] G. L. Brennecka, W. Huebner, B. A. Tuttle, and P. G. Clem, "Use of stress to produce highly oriented tetragonal lead zirconate titanate (PZT 40/60) thin films and resulting electrical properties," *J. Am. Ceram. Soc.*, vol. 87, pp. 1459–1465, Aug. 2004, doi: 10.1111/j.1551-2916.2004.01459.

[12] *FRAM Guide Book*, Fujitsu, Tokyo, Japan, 2010.

[13] A. Pramanick, A. D. Prewitt, J. S. Forrester, and J. L. Jones, "Domains, domain walls and defects in perovskite ferroelectric oxides: A review of present understanding and recent contributions," *Crit. Rev. Solid State Mater. Sci.*, vol. 37, no. 4, pp. 243–275, Dec. 2012, doi: 10.1080/10408436.2012.686891.

[14] F. Griggio *et al.*, "Substrate clamping effects on irreversible domain wall dynamics in lead zirconate titanate thin films," *Phys. Rev. Lett.*, vol. 108, no. 15, Apr. 2012, doi: 10.1103/PhysRevLett.108.157604.

[15] R. J. Ong, D. A. Payne, and N. R. Sottos, "Processing effects for integrated PZT: Residual stress, thickness, and dielectric properties," *J. Amer. Ceram. Soc.*, vol. 88, no. 10, pp. 2839–2847, Oct. 2005, doi: 10.1111/j.1551-2916.2005.00641.x.

[16] W. Pompe, X. Gong, Z. Suo, and J. S. Speck, "Elastic energy release due to domain formation in the strained epitaxy of ferroelectric and ferroelastic films," *J. Appl. Phys.*, vol. 74, no. 10, pp. 6012–6019, Nov. 1993, doi: 10.1063/1.355215.

[17] E. B. Araújo, E. C. Lima, I. K. Bdikin, and A. L. Kholkin, "Thickness dependence of structure and piezoelectric properties at nanoscale of polycrystalline lead zirconate titanate thin films," *J. Appl. Phys.*, vol. 113, no. 18, May 2013, Art. no. 187206, doi: 10.1063/1.4801961.
[18] E. Hong, R. Smith, S. V. Krishnaswamy, C. B. Freidhoff, and S. Trolier-McKinstry, "Residual stress development in Pb(zr,Ti)O_3/zrO_2/SiO_2 stacks for piezoelectric microactuators," *Thin Solid Films*, vol. 510, nos. 1–2, pp. 213–221, Jul. 2006, doi: 10.1016/j.tsf.2005.12.300.
[19] B. Ma *et al.*, "Residual stress of $(Pb_{0.92}La_{0.08})(Zr_{0.52}Ti_{0.48})O_3$ films grown by a sol–gel process," *Smart Mater. Struct.*, vol. 22, no. 5, May 2013, Art. no. 055019, doi: 10.1088/0964-1726/22/5/055019.
[20] Y. Bastani, T. Schmitz-Kempen, A. Roelofs, and N. Bassiri-Gharb, "Critical thickness for extrinsic contributions to the dielectric and piezoelectric response in lead zirconate titanate ultrathin films," *J. Appl. Phys.*, vol. 109, no. 1, Jan. 2011, Art. no. 014115, doi: 10.1063/1.3527970.
[21] L. M. Denis, G. Esteves, J. Walker, J. L. Jones, and S. Trolier-McKinstry, "Thickness dependent response of domain wall motion in declamped 001 Pb $(Zr_{0.3}Ti_{0.7})$ O_3 thin films," *Acta Mater.*, vol. 151, pp. 243–252, Jun. 2018, doi: 10.1016/j.actamat.2018.03.046.
[22] C.-R. Cho, W.-J. Lee, B.-G. Yu, and B.-W. Kim, "Dielectric and ferroelectric response as a function of annealing temperature and film thickness of sol-gel deposited $Pb(Zr_{0.52}Ti_{0.48})O_3$ thin film," *J. Appl. Phys.*, vol. 86, no. 5, pp. 2700–2711, Sep. 1999, doi: 10.1063/1.371114.
[23] N. Bassiri-Gharb, I. Fujii, E. Hong, S. Trolier-McKinstry, D. V. Taylor, and D. Damjanovic, "Domain wall contributions to the properties of piezoelectric thin films," *J. Electroceram.*, vol. 19, no. 1, pp. 49–67, Oct. 2007, doi: 10.1007/s10832-007-9001-1.
[24] D.-J. Kim *et al.*, "Thickness dependence of submicron thick $Pb(Zr_{0.3}Ti_{0.7})O_3$ films on piezoelectric properties," *Ceram. Int.*, vol. 34, no. 8, pp. 1909–1915, Dec. 2008, doi: 10.1016/j.ceramint.2007.07.016.
[25] J. I. Yang, R. G. Polcawich, L. M. Sanchez, and S. Trolier-McKinstry, "Effect of feature size on dielectric nonlinearity of patterned $PbZr_{0.52}Ti_{0.48}O_3$ films," *J. Appl. Phys.*, vol. 117, no. 1, Jan. 2015, Art. no. 014103, doi: 10.1063/1.4905300.
[26] S. Trolier-McKinstry, N. Bassiri Gharb, and D. Damjanovic, "Piezoelectric nonlinearity due to motion of 180° domain walls in ferroelectric materials at subcoercive fields: A dynamic poling model," *Appl. Phys. Lett.*, vol. 88, no. 20, May 2006, Art. no. 202901, doi: 10.1063/1.2203750.
[27] K. S. Lee, Y. K. Kim, S. Baik, J. Kim, and I. S. Jung, "*In situ* observation of ferroelectric 90°-domain switching in epitaxial Pb(zr, Ti)O_3 thin films by synchrotron X-ray diffraction," *Appl. Phys. Lett.*, vol. 79, no. 15, pp. 2444–2446, Oct. 2001, doi: 10.1063/1.1406981.
[28] R. L. Johnson-Wilke *et al.*, "Ferroelectric/Ferroelastic domain wall motion in dense and porous tetragonal lead zirconate titanate films," *IEEE Trans. Ultrason., Ferroelectr., Freq. Control*, vol. 62, no. 1, pp. 46–55, Jan. 2015, doi: 10.1109/TUFFC.2014.006562.
[29] M. Wallace *et al.*, "*In situ* measurement of increased ferroelectric/ferroelastic domain wall motion in declamped tetragonal lead zirconate titanate thin films," *J. Appl. Phys.*, vol. 117, no. 5, Feb. 2015, Art. no. 054103, doi: 10.1063/1.4907394.
[30] S. Li, A. S. Bhalla, R. E. Newnham, L. E. Cross, and C.-Y. Huang, "90‡ domain reversal in $Pb(ZrxTi_{1-x})O_3$ ceramics," *J. Mater. Sci.*, vol. 29, no. 5, pp. 1290–1294, 1994, doi: 10.1007/BF00975077.
[31] G. Esteves *et al.*, "Effect of mechanical constraint on domain reorientation in predominantly 111-textured lead zirconate titanate films," *J. Amer. Ceram. Soc.*, vol. 99, no. 5, pp. 1802–1807, May 2016, doi: 10.1111/jace.14159.
[32] A. Bernal, A. Tselev, S. Kalinin, and N. Bassiri-Gharb, "Free-standing ferroelectric nanotubes processed via soft-template infiltration," *Adv. Mater.*, vol. 24, no. 9, pp. 1160–1165, Mar. 2012, doi: 10.1002/adma.201103993.
[33] S. S. N. Bharadwaja, M. Olszta, S. Trolier-McKinstry, X. Li, T. S. Mayer, and F. Roozeboom, "Fabrication of high aspect ratio ferroelectric microtubes by vacuum infiltration using macroporous silicon templates," *J. Amer. Ceram. Soc.*, vol. 89, pp. 2695–2701, May 2006, doi: 10.1111/j.1551-2916.2006.01123.x.
[34] R. Keech *et al.*, "Declamped piezoelectric coefficients in patterned 70/30 lead magnesium niobate-lead titanate thin films," *Adv. Funct. Mater.*, vol. 27, no. 9, Mar. 2017, Art. no. 1605014, doi: 10.1002/adfm.201605014.
[35] N. Ledermann *et al.*, "1 0 0-Textured, piezoelectric Pb (Zrx, Ti_{1-x}) O_3 thin films for MEMS: Integration, deposition and properties," *Sens. Actuators A, Phys.*, vol. 105, pp. 162–170, Jul. 2003, doi: 10.1016/S0924-4247(03)00090-6.
[36] S. K. Dey, K. D. Budd, and D. A. Payne, "Thin-film ferroelectrics of PZT of sol-gel processing," *IEEE Trans. Ultrason., Ferroelectr., Freq. Control*, vol. 35, no. 1, pp. 80–81, Jan. 1988, doi: 10.1109/58.4153.
[37] A. Berger, M. Herwegh, J.-O. Schwarz, and B. Putlitz, "Quantitative analysis of crystal/grain sizes and their distributions in 2D and 3D," *J. Struct. Geol.*, vol. 33, no. 12, pp. 1751–1763, Dec. 2011, doi: 10.1016/j.jsg.2011.07.002.
[38] F. K. Lotgering, "Topotactical reactions with ferrimagnetic oxides having hexagonal crystal structures—I," *J. Inorg. Nucl. Chem.*, vol. 9, pp. 113–123, Feb. 1959, doi: 10.1016/0022-1902(59)80070-1.
[39] A. P. Hammersley, S. O. Svensson, M. Hanfland, A. N. Fitch, and D. Hausermann, "Two-dimensional detector software: From real detector to idealised image or two-theta scan," *High Pressure Res.*, vol. 14, nos. 4–6, pp. 235–248, Jan. 1996, doi: 10.1080/08957959608201408.
[40] G. Esteves, K. Ramos, C. M. Fancher, and J. L. Jones, "LIPRAS: Line-profile analysis software," GitHub, North Carolina State Univ., Raleigh, NC, USA, Tech. Rep., 2017, pp. 1–4, doi: 10.13140/RG.2.2.29970.25282/3.
[41] J. E. Daniels, J. L. Jones, and T. R. Finlayson, "Characterization of domain structures from diffraction profiles in tetragonal ferroelastic ceramics," *J. Phys. D, Appl. Phys.*, vol. 39, no. 24, pp. 5294–5299, Dec. 2006, doi: 10.1088/0022-3727/39/24/029.
[42] J. L. Jones, E. B. Slamovich, and K. J. Bowman, "Domain texture distributions in tetragonal lead zirconate titanate by X-ray and neutron diffraction," *J. Appl. Phys.*, vol. 97, no. 3, Feb. 2005, Art. no. 034113, doi: 10.1063/1.1849821.
[43] T. Key, J. L. Jones, W. F. Shelley, and K. J. Bowman, "Quantifying domain textures in lead zirconate titanate using 022: 202 and 220 diffraction peaks," *Solid State Phenom.*, vol. 105, pp. 379–384, Jul. 2005, doi: 10.4028/www.scientific.net/SSP.105.379.
[44] *International Centre for Diffraction Data, in Card 01-070-4261, (n.d.)*, ICDD, Newtown Square, PA, USA.
[45] M. J. Haun, E. Furman, S. J. Jang, and L. E. Cross, "Thermodynamic theory of the lead zirconate-titanate solid solution system, part V: Theoretical calculations," *Ferroelectrics*, vol. 99, no. 1, pp. 63–86, Nov. 1989, doi: 10.1080/00150198908221440.
[46] V. Lantto, J. Lappalainen, and M. Kakihana, "Phase transitions of $Pb(Zr_xTi_{1-x})O_3$ ceramics," *Phys. Rev. B, Condens. Matter.*, vol. 66, pp. 1–15, Aug. 2002, doi: 10.1103/PhysRevB.66.064108.
[47] Y. Ehara *et al.*, "*In-situ* observation of ultrafast 90° domain switching under application of an electric field in (100)/(001)-oriented tetragonal epitaxial $Pb(Zr_{0.4}Ti_{0.6})O_3$ thin films," *Sci. Rep.*, vol. 7, no. 1, pp. 1–7, Dec. 2017, doi: 10.1038/s41598-017-09389-6.
[48] W. Cao and C. A. Randall, "Grain size and domain size relations in bulk ceramic ferroelectric materials," *J. Phys. Chem. Solids.*, vol. 57, pp. 1499–1505, Oct. 1996, doi: 10.1016/0022-3697(96)00019-4.

Lyndsey M. Denis-Rotella (Member, IEEE) received the B.S. degree in chemical engineering from the University of Florida, Gainesville, FL, USA, in 2014 and the Ph.D. degree in materials science and engineering from Pennsylvania State University, University Park, PA, USA, in 2019, under the group of Prof. S. Trolier-McKinstry.

During her graduate studies, she focused on the investigation of mechanisms that govern property degradation in ferroelectric materials that are scaled-down for industrial use, such as low-power sensors, actuators, and general microelectromechanical systems (MEMS). Recently, she completed a Naval Research Enterprise Internship Program in the Materials Science & Technology Division, conducting research on the mechanical, electrical, and magnetic properties of Mn-doped relaxor ferroelectric multiferroic crystals for transducer applications.

Dr. Denis-Rotella was awarded the NSF Graduate Research Fellowship in 2015 and became an Alfred P. Sloan Minority Graduate Scholar in 2017.

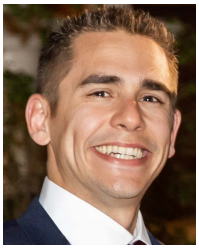

Giovanni Esteves received the B.S.E. degree in chemical engineering from Arizona State University, Tempe, AZ, USA, in 2012 and the Ph.D. degree in materials science and engineering from North Carolina State University, Raleigh, NC, USA, in 2017.

He is currently a Research and Development Electronics Engineer with MESA Complex at Sandia National Laboratory (SNL), Albuquerque, NM, USA. During his graduate studies, he developed structure–property relationships of ferroelectric thin films by studying their response *in situ* with high-brilliance X-ray diffraction. He is currently a Key Contributor to Sandia's piezoelectric microelectromechanical systems (piezoMEMS) Program, which actively fabricates and researches ultrasonic transducers, piezoelectric resonators, and RF filter technologies. His research interests include ferroelectrics, piezoelectrics, crystallography, and piezoMEMS.

Julian Walker received the B.S. degree in ceramic engineering from the University of New South Wales, and the Ph.D. degree in materials science and engineering from the University of New South Wales, Sydney, NSW, Australia, in 2014, under the group of Prof. N. Valanoor.

He was a Postdoctoral Researcher with Electronic Ceramics Department, Jozef Stefan Institute, Ljubljana, Slovenia, with Prof. B. Malic working on lead-free piezoceramics, from 2014 to 2016. He then became a member of Prof. S. Trolier-McKinstry's Research Group, Materials Research Institute, Pennsylvania State University, University Park, PA, USA, from 2016 to 2018, where he worked with piezoelectric thin film application and innovation. He is currently a Postdoctoral Fellow with Functional Materials and Materials Chemistry Research Group (FACET), Department of Materials Science and Engineering, Norwegian University of Science and Technology (NTNU), Trondheim, Norway. His current research push is on functional supramolecular materials and plastic crystal ferroics.

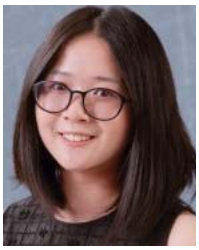

Hanhan Zhou (Associate Member, IEEE) received the B.S. degree in materials science and engineering from Purdue University, West Lafayette, IN, USA, in 2014 and the Ph.D. degree in materials science and engineering from North Carolina State University, Raleigh, NC, USA, in 2019.

She was a Postdoctoral Researcher with Analytical Instrumentation Facility (AIF), North Carolina State University, until 2020. She is currently a Sr. Electrical Failure and Package Failure Analysis Engineer with Global Foundries, Malta, NY, USA. During her graduate studies, her research interests included radiation hardness in multifunctional micro-/nanoelectromechanical (MEMS) devices. She currently performs complex failure analysis on the nanolevel to improve package quality and reliability.

Jacob L. Jones (Fellow, IEEE) is currently a Professor of materials science and engineering, the Director and the Principal Investigator of the research triangle nanotechnology network (RTNN), the Director of the Analytical Instrumentation Facility (AIF), and a University Faculty Scholar with North Carolina State University (NC State), Raleigh, NC, USA. His research interests involve developing structure–property-processing relationships in emerging functional materials, primarily through the use of advanced X-ray and neutron scattering tools. He has authored over 250 articles on these topics.

Prof. Jones is a fellow of the American Ceramic Society. He is the Vice-President for Ferroelectrics in the IEEE Ultrasonics, Ferroelectrics, and Frequency Control (UFFC) Society. He has received numerous awards for his research and education activities, including the Presidential Early Career Award for Scientists and Engineers (PECASE), the IEEE UFFC Ferroelectrics Young Investigator Award, the NC State College of Engineering George H. Blessis Outstanding Undergraduate Advisor Award, and the 2019 Alumni Association Outstanding Research Award at NC State.

Susan Trolier-McKinstry (Fellow, IEEE) is currently the Steward S. Flaschen Professor of ceramic science and engineering, a Professor of electrical engineering, and the Director of the Nanofabrication Facility, Pennsylvania State University, University Park, PA, USA. Her main research interest includes thin films for dielectric and piezoelectric applications.

Prof. Trolier-McKinstry is a member of the National Academy of Engineering, a fellow of the American Ceramic Society and the Materials Research Society, and an Academician of the World Academy of Ceramics. She currently serves as an Associate Editor for *Applied Physics Letters*. She was the 2017 President of the Materials Research Society and previously she served as the President of the IEEE Ultrasonics, Ferroelectrics and Frequency Control Society and Keramos. Twenty-one people whom she has advised/co-advised have gone on to take faculty positions around the world.